Research Article | Vol. 25, No. 23 | 13 Nov 2017 | OPTICS EXPRESS 29296
Optics EXPRESS

Hollow-core air-gap anti-resonant fiber couplers

XIAOSHENG HUANG, JIE MA, DINGYUAN TANG, AND SEONGWOO YOO*

The Photonics Institute, School of Electrical and Electronic Engineering, Nanyang Technological University, 50 Nanyang Avenue, Singapore 639798, Singapore
*seon.yoo@ntu.edu.sg

Abstract: We design, fabricate, and demonstrate the first hollow-core air-gap anti-resonant fiber coupler in a dual hollow-core anti-resonant fiber (DHAF) structure. The coupling takes place through an air gap between air cores, promising a limitless operation window beyond material transmission. The DHAF follows the same waveguide mechanism as the hollow-core anti-resonant fiber (HAF). The coupling is attainable over the entire transmission bands determined by a resonant frequency of a HAF. A coupling length, thus coupling strength, is controllable by adjusting fiber design parameters. In addition, at a fixed design and length, the coupling strength linearly responds to longitudinal mechanical tension, enabling continuous variable coupling ratio in a single coupler. Furthermore, we confirm that the coupler is polarization insensitive, and does not require precise polarization alignment of an input beam. We demonstrate its robust coupling performance and applicability in forming a fiber laser ring cavity, and delivering and power splitting ultrafast laser pulse. The air-core air-gap coupling promises applications in mid-infrared and ultraviolet regions where the current coupling technology is limited.

OCIS codes: (060.2280) Fiber design and fabrication; (060.5295) Photonic crystal fibers; (140.3070) Infrared and far-infrared lasers; (320.7080) Ultrafast devices.

References and links

1. F. Couny, F. Benabid, P. Roberts, P. Light, and M. Raymer, "Generation and photonic guidance of multi-octave opticalfrequency combs," Science **318**(5853), 1118–1121 (2007).
2. X. Huang, S. Yoo, and K. T. Yong, "Function of second cladding layer in hollow core tube lattice fibers," Sci. Rep. **7**, 1618 (2017).
3. F. Poletti, "Nested antiresonant nodeless hollow core fiber," Opt. Express **22**(20), 23807–23828 (2014).
4. F. Yu and J. Knight, "Negative curvature hollow core optical fiber," IEEE J. Sel. Topics Quantum Electron. **22**(2), 1–11 (2016).
5. X. Huang, W. Qi, D. Ho, K. T. Yong, F. Luan, and S. Yoo, "Hollow core anti-resonant fiber with split cladding," Opt. Express **24**(7), 7670–7678 (2016).
6. J. R. Hayes, S. R. Sandoghchi, T. D. Bradley, Z. Liu, R. Slavík, M. A. Gouveia, N. V. Wheeler, G. Jasion, Y. Chen, E. N. Fokoua, M. N. Petrovich, D. J. Richardson, and F. Poletti, "Antiresonant hollow core fiber with an octave spanning bandwidth for short haul data communications," J. Lightwave Technol. **35**(3), 437–442 (2017).
7. B. Debord, A. Amsanpally, M. Chafer, A. Baz, M. Maurel, J. Blondy, E. Hugonnot, F. Scol, L. Vincetti, F. Gérôme, and F. Benabid, "Ultralow transmission loss in inhibited-coupling guiding hollow fibers," Optica **4**(2), 209–217 (2017).
8. F. Yu, W. J. Wadsworth, and J. C. Knight, "Low loss silica hollow core fibers for 3–4 mm spectral region," Opt. Express **20**(10), 11153–11158 (2012).
9. M. R. A. Hassan, F. Yu, W. J. Wadsworth, and J. C. Knight, "Cavity-based mid-IR fiber gas laser pumped by a diode laser," Optica **3**(3), 218–221 (2016).
10. B. Wedel and M. Funck, "Industrial fiber beam delivery system for ultrafast lasers," Laser Technik Journal **13**(4), 42–44 (2016).
11. F. Benabid, J. C. Knight, G. Antonopoulos, and P. S. J. Russell, "Stimulated Raman scattering in hydrogen-filled hollowcore photonic crystal fiber," Science **298**(5592), 399–402 (2002).
12. A. Argyros, S. G. Leon-Saval, and M. A. van Eijkelenborg, "Twin-hollow-core optical fibres," Opt. Commun. **282**(9), 1785–1788 (2009).
13. N. Wheeler, T. Bradley, J. Hayes, G. Jasion, Y. Chen, S. Sandoghchi, P. Horak, F. Poletti, M. Petrovich, and D. Richardson, "Dual hollow-core anti-resonant fibres," Proc. SPIE **9886**, 988617 (2016).

#306921 https://doi.org/10.1364/OE.25.029296
Journal © 2017 Received 12 Sep 2017; revised 2 Nov 2017; accepted 2 Nov 2017; published 9 Nov 2017

Optics EXPRESS

14. L. Meng, J. Fini, J. Nicholson, R. Windeler, A. DeSantolo, E. Monberg, F. DiMarcello, M. Hassan, and R. Ortiz, "Bend tunable coupling in dual-hollow-core photonic bandgap fiber," in Optical Fiber Communication Conference and Exposition and the National Fiber Optic Engineers Conference (OFC/NFOEC). (IEEE, 2012), pp. 1–3.
15. Z. Xu, X. Li, C. Zhang, W. Ling, P. Liu, L. Xia, and H. Yang, "Design of single-polarization coupler based on dual-core photonic band-gap fiber implied in resonant fiber optic gyro," Opt. Commun. **380**, 302–309 (2016).
16. W. Belardi and J. C. Knight, "Effect of core boundary curvature on the confinement losses of hollow antiresonant fibers," Opt. Express **21**(19), 21912–21917 (2013).
17. Y. Wang, N. V. Wheeler, F. Couny, P. Roberts, and F. Benabid, "Low loss broadband transmission in hypocycloid-core Kagome hollow-core photonic crystal fiber," Opt. Lett. **36**(5), 669–671 (2011).
18. X. Liu, Z. Fan, Z. Shi, Y. Ma, J. Yu, and J. Zhang, "Dual-core antiresonant hollow core fibers," Opt. Express **24**(15), 17453–17458 (2016).
19. G. Stevens and T. Woodbridge, "Mid-IR fused fiber couplers," Proc. SPIE **9730**, 973007 (2016).
20. I. Ishida, T. Akamatsu, Z. Wang, Y. Sasaki, K. Takenaga, and S. Matsuo, "Possibility of stack and draw process as fabrication technology for multi-core fiber," in Optical Fiber Communication Conference and Exposition and the National Fiber Optic Engineers Conference (OFC/NFOEC). (IEEE, 2013), pp. 1–3.
21. Y. Jung, G. Brambilla, and D. J. Richardson, "Optical microfiber coupler for broadband single-mode operation," Opt. Express **17**(7), 5273–5278 (2009).
22. L. Vincetti and V. Setti, "Confinement loss in Kagome and tube lattice fibers: comparison and analysis," J. Lightwave Technol. **30**(10), 1470–1474 (2012).
23. Z. Wang, G. Kai, Y. Liu, J. Liu, C. Zhang, T. Sun, C. Wang, W. Zhang, S. Yuan, and X. Dong, "Coupling and decoupling of dual-core photonic bandgap fibers," Opt. Lett. **30**(19), 2542–2544 (2005).
24. M. Pang, H. Xuan, J. Ju, and W. Jin, "Influence of strain and pressure to the effective refractive index of the fundamental mode of hollow-core photonic bandgap fibers," Opt. Express **18**(13), 14041–14055 (2010).
25. F. Luan, J. Knight, P. S. J. Russell, S. Campbell, D. Xiao, D. Reid, B. Mangan, D. Williams, and P. Roberts, "Femtosecond soliton pulse delivery at 800nm wavelength in hollowcore photonic bandgap fibers," Opt. Express **12**(5), 835–840 (2004).
26. J. Ma, H. Huang, K. Ning, X. Xu, G. Xie, L. Qian, K. P. Loh, and D. Tang, "Generation of 30 fs pulses from a diodepumped graphene mode-locked Yb : $CaYAlO_4$ laser," Opt. Lett. **41**(5), 890–893 (2016).
27. G. P. Agrawal, *Nonlinear Fiber Optics* (Academic, Boston, 2007).
28. S. Zahedpour, J. Wahlstrand, and H. Milchberg, "Measurement of the nonlinear refractive index of air constituents at mid-infrared wavelengths," Opt. Lett. **40**(24), 5794–5797 (2015).
29. D. Li, J. Feng, and D. Pacifici, "Nanoscale optical interferometry with incoherent light," Sci. Rep/. **6**, 20836 (2016).
30. I. I. Faruque, D. Bonneau, G. F. Sinclair, and M. G. Thompson, "Heralded Quantum Interference of On-chip Micro-ring Resonator Sources in Si-photonics," in CLEO: QELS_Fundamental Science (Optical Society of America, 2017), paper JTh3E–3.
31. D. Huang, E. A. Swanson, C. P. Lin, J. S. Schuman, W. G. Stinson, W. Chang, M. R. Hee, T. Flotte, K. Gregory, C. A. Puliafito, and J. G. Fujimoto, "Optical coherence tomography," Science **254**(5035), 1178–1181 (1991).
32. Corning Incorporated, "Corning 62.5/125 Optical Fiber Product Information," http://www.photonics.byu.edu/FiberOpticConnectors.parts/images/mmf625.pdf.

1. Introduction

Hollow-core anti-resonant fibers (HAFs) become one of the most popular air core fiber designs, with properties of multiple broad transmission bands [1, 2], simple and flexible cladding structures [3–5], and relatively low transmission loss [6, 7]. The air core guidance opens up a new route to deliver mid-IR [8, 9] as well as ultrafast pulses [10]. While the majority of work related to HAFs has been focused on geometries with a single core within the cladding structure [11], a dual core HAF is promising to serve as a hollow-core fiber coupler that inherits the properties of HAF. However, most of prior dual core HAF designs possess cladding struts between the cores [12, 13] (also true for other dual hollow-core fibers [14, 15]). Consequently, the core mode must transverse the cladding material to transfer its power, and thus, suffering material limitations of the cladding. Hence, the cladding struts located between the air cores sacrifice the advantages of air-core guidance. More importantly, the cladding struts separating the air core induce strong modal confinement in the core and inhibit the formation of supermodes, and thus, preventing the mode coupling between cores [12]. In [13], although mode coupling between the dual core was observed by flatting out the silica wall, which weakens modal confinement [16, 17], the coupling performance showed drawbacks such as limited achievable coupling strength, wavelength sensitive coupling strength, polarization dependent coupling strength, and relatively high transmission

Optics EXPRESS

loss ($> 1dB/m$). To maximize the air core benefits and improve the coupling performance, it is desired to replace the solid wall with an air layer between air cores. Subsequently, in [18], a dual core bridged by an air channel was theoretically investigated as a dual core HAF. The study suggested light coupling through the air channel, which is polarization independent with a relative low transmission loss at $0.1dB/m$ level. However, the proposed elliptical design deems impractical for fabrication. On the other hand, we note prior efforts on developing of a mid-IR fused fiber coupler via fusing and stretching ZBLAN or chalcogenide fibers [19]. Challenges in obtaining reliable mid-IR coupler, with this approach, arose from weak physical strength of the soft glass fibers. The fibers broke while being stretched, resulting in short fused length and partial coupling. In contrast, an air-core air-gap fiber coupler can reach to the mid-IR without the material restriction.

In this presented work, we report, for the first time, demonstration of robust air-core air-gap light coupling in a DHAF, based on our anti-resonant design [2, 5]. The DHAF is directly drawn using the conventional fiber drawing tower, thus enabling continuous volume fabrication. The developed DHAF inherits the anti-resonant guiding mechanism of a single core HAF. Hence, transmission band is readily tuned for application wavelengths unlimited by material transmission. Its coupling strength is controllable by adjusting design parameters. More interestingly, the coupling strength is linearly variable with a longitudinal tension, and the entire anti-resonant transmission band is coupled. This is an important aspect for ultrafast pulse coupling. The robust coupling mechanism is verified, being implemented as an output fiber coupler in a laser ring cavity. Moreover, the DHAF retains the superiority of air-core anti-resonant guidance which is proved by delivering and splitting a 47 fs laser pulse without inducing any significant pulse broadening. Therefore, our DHAF has the potentials to work as a mid-IR and ultrafast fiber coupler.

2. DHAF design and characterization

As shown in Fig. 1(a), our DHAF design composes of two hollow cores, **1**, which are connected through an air gap, **3**. One layer of cladding capillaries, **2**, surrounds the hollow cores to form an anti-resonant waveguide. The external cladding is constructed with rods to ease fabrication complexity. The DHAF fabricated by the stack and draw technique [20] is presented in Fig. 1(b). The fabricated DHAF has a good structure that verifies the novelty and practicality of our design.

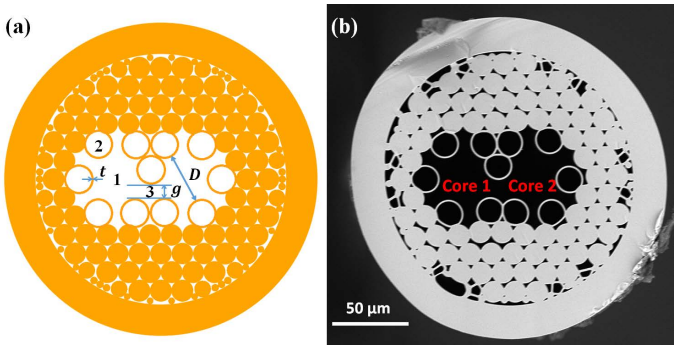

Fig. 1. (a) Designed structure of DHAF, t is capillary wall thickness, g is air gap width, and D is core diameter. (b) Cross sectional view of a fabricated DHAF, in which $t = 1.21\mu m$, $D = 35.2\mu m$ and $g = 11.5\mu m$.

The transmission properties witness the anti-resonant characteristics of DHAF as presented in Fig. 2(a). Core 1, as shown in Fig.1(b), is served as an input port and the transmission spectrum is measured at both core 1 and core 2. For both transmission spectra collected from

Optics EXPRESS

core 1 and core 2, the transmission bands are determined by the normalized frequency, F, confirming its anti-resonant property. The fine oscillation feature of the spectrum attributes to modal interference between the lower-order symmetric and anti-symmetric supermodes of coupling [21]. Both the period and strength of the sinusoidal modulation in the transmission spectrum increase as the coupler length gets shorter, as indicated by Fig. 2(b), which manifests itself as supermode interference. The regular oscillation pattern from 1450 *nm* to 1700 *nm* indicates that the fundamental mode is dominant in the DHAF. In the wavelengths (from 1320 *nm* to 1450 *nm*) close to the resonant wavelength region, the irregular oscillation indicates the multimode transmission [21].

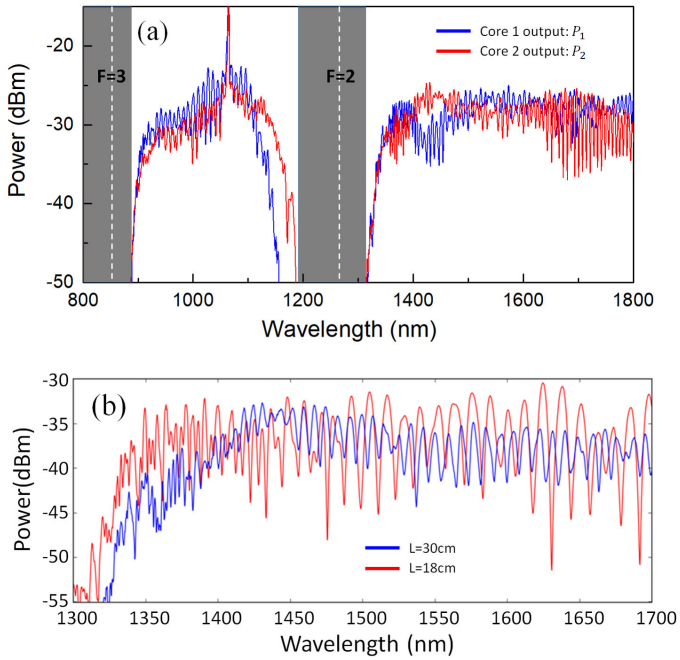

Fig. 2. (a)Transmission spectra collected from core 1 and core 2 when light is coupled into core 1 of the DHAF in Fig. 1(b). Transmission bands are determined by the normalized frequency [22], $F = 2t\sqrt{n^2 - 1}/\lambda$, where n is the refractive index of cladding material (1.45) and λ is the wavelength. Shaded areas correspond to high resonant regions. (b) Output spectra from the core 2 of DHAF at different lengths.

In a dual-core fiber, energy is transferred between the cores in a sinusoidal form along the fiber. The shortest length at which optical power is totally transferred to the neighboring core is defined as a coupling length [18, 23], denoted as L_c. The coupling length is defined by $L_c = \frac{\lambda}{2\Delta n}$, where Δn is the effective refractive index difference between the first order symmetric and antisymmetric modes [23]. In our DHAF structure, the coupling length L_c can be controlled by design parameters, g and D. We use Comsol Multiphysics to calculate the Δn. The calculated L_c is presented in Fig. 3(a), showing linear dependence of the L_c on the air gap width, g, when core diameter, D, keeps invariant. For a DHAF with $g = 11.5\mu m$, the L_c is measured to be 35 *cm* from the evolution of the coupling ratio along the length of the DHAF (see Fig. 3(b)). The coupling ratio is measured following $P_2/(P_1 + P_2)$, where P_1 and P_2 are the output power from core 1 and core 2, respectively, when input power, P, is launched into the core 1. Subsequently, the excess loss is determined by $-10log\frac{P_1+P_2}{P}$. The theoretical result is well matched with a measured value within 8% discrepancy. Hence, the L_c dependence on the design parameters offers a new degree of freedom in determining a coupling strength in addition to the coupler

Optics EXPRESS

length as commonly practiced in a fused fiber coupler.

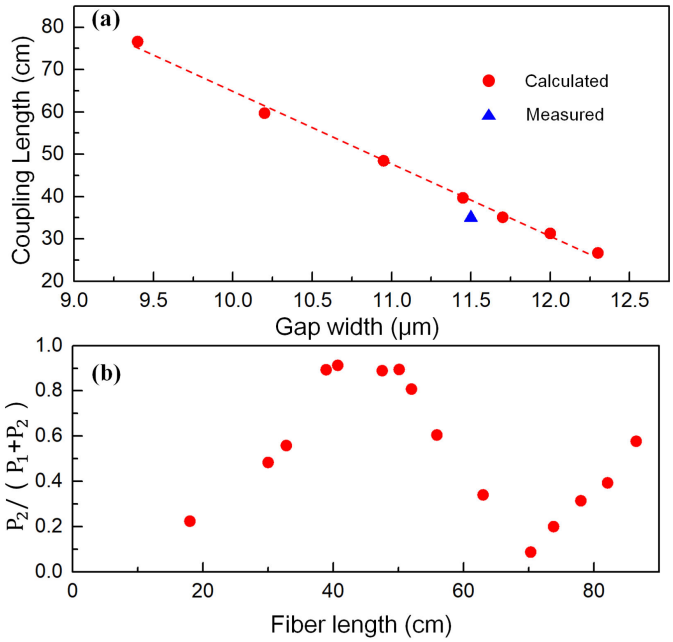

Fig. 3. Coupling length of DHAF decreases linearly (as indicated by the red dashed line) as air gap width gets wider. The measurement is consistent with the calculation. (b) Evolution of the measured coupling ratio along DHAF length. The coupling ratio is measured under tension. The DHAF has a gap width $g = 11.5\mu m$. (For both (a) and (b), $D = 35cm$, $\lambda = 1060nm$)

In addition to the design parameter dependence, more interestingly, the coupling strength of the DHAF is variable by applying longitudinal tension even at a fixed design and length. This variable coupling ratio is demonstrated in Fig. 4. The coupler is mounted on translational stages. Incident light at 1.06 μm wavelength is launched into the core 1, and output lights from both cores are monitored with a charged coupled device (CCD) camera to evaluate the coupling performance. The coupler length is chosen at 40 cm, matched to the coupling length as indicated in Figs. 3(a) and 3(b). The tension applied on the fiber can be represented by the longitudinal travelling distance of the translation stage. To evaluate the variable coupling ratio and its excess loss, the DHAF is placed in a straight way between two translation stages. When no additional tension is applied, the coupling ratio is small around 5% despite the fiber length matches to L_c. The ratio, however, linearly increases from 5% to 95% by stretching the fiber by 40 μm, and linearly returns to the initial coupling ratio when tension is released. The linear variable coupling strength is repeatable. To the best of our knowledge, this is the first demonstration of a variable coupling effect in a DHAF. Near field mode patterns from the output ports at different tensions are also shown in Fig. 4, evidencing the variable coupling ratios (see Visualization 1 and Visualization 2). Moreover, the variable coupling does not deteriorate a fiber excess loss. As presented with a red line in Fig. 4, the excess loss is consistently measured at 0.35 dB over the entire coupling ratio. We also note that the transmission anti-resonant bands remain intact with the various tensions (see Appendix A).

We speculate that the dependence of the coupling ratio on the longitudinal tension is related to phase sensitivity of the fundamental mode to strain. As reported in [24], longitudinal strain can induce structural deformation of the hollow core fiber, resulting in fundamental mode effective index change. Moreover, in our DHAF, the strain induced structural deformation can change the

Optics EXPRESS

gap width, which would greatly influence the coupling length as indicated in Fig. 3(a).

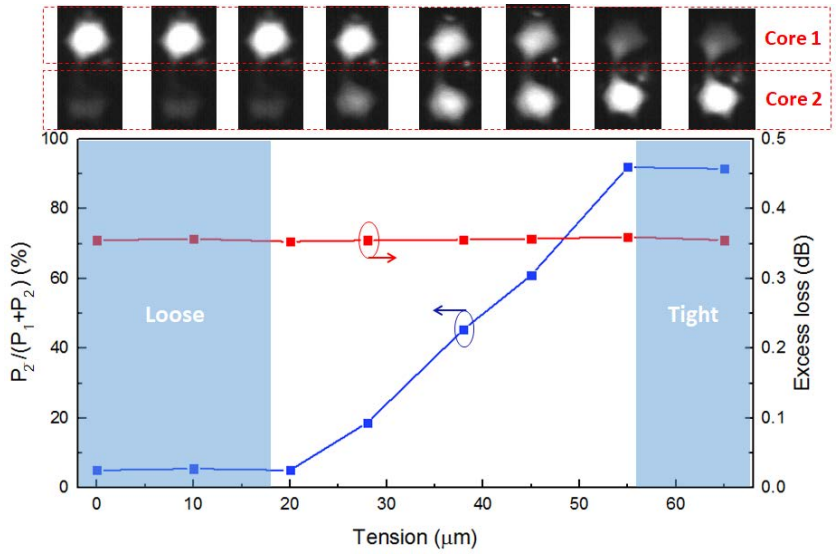

Fig. 4. Linear variation of the coupling ratio (blue lines) on external tension. The corresponding excess loss (red lines) is also presented. The fiber has a structure as shown in Fig. 1(b). The fiber length is 40 *cm* and the wavelength is 1060 *nm*. The near filed mode images show the energy distribution under different tensions.

We further investigate the coupling performance in an aspect of polarization dependence. An input light at 980 *nm* gets linearly polarized via a linear polarizer placed in front of the coupler. The polarized beam is then coupled into the core 1 of a DHAF. The transmitted powers at core 1 and core 2 are measured with a power meter, denoted as P_1 and P_2, respectively. As summarized in Table 1, the coupling ratio is maintained while rotating the polarization of input light, which confirms polarization independent performance of our coupler. The variant power readings of P_1 and P_2 account for original polarization of the input light. The input power attenuates when its polarization is not aligned to the linear polarizer. The property of polarization independent can get rid of the tedious process of input beam polarization alignment to a fiber polarization axis, hence making the coupler's applications broader.

Table 1. Polarization and Coupling Ratio

$\triangle\theta$	0^o	30^o	60^o	90^o	120^o	150^o
$P_1(mW)$	43	30	6.5	-	13.5	31
$P_2(mW)$	26	19	4	-	8.5	19
$P_2/(P_1+P_2)$	0.38	0.39	0.38	-	0.39	0.38

$\triangle\theta$: Angle difference between the directions of the linear polarizer and the incident light polarization.

3. Applications of DHAF

To validate applicability of our DHAF, we construct a ytterbium doped fiber (YDF) laser ring cavity using our DHAF as a variable output coupler. The setup configuration is depicted in Fig. 5. A 980*nm* pump beam is coupled into the ring cavity via a commercial wavelength division multiplexing (WDM) coupler. Signal light generated in the YDF is coupled out from the ring cavity via the DHAF. The output coupling (OC) ratio ($r = P_2/(P_1+P_2)$) is adjustable by applying

Optics EXPRESS

longitudinal strain on the DHAF. The variable OC ratio enables us to maximize the output power without physically changing the output coupler.

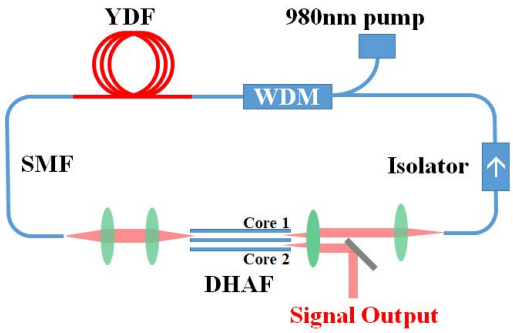

Fig. 5. Experimental layout of the laser cavity. YDF: Ytterbium-doped fiber, SMF: Single mode fiber.

The cavity was successfully lasing with our coupler. When the OC ratio is set at a 17%, output power of 27 mW at 1057 nm was recorded with a 10% of slope efficiency as shown in Fig. 6. The output power grows with the increasing OC until it reaches the maximum output power. Figure 7 represents the benefit of using the variable output coupler for cavity optimization. The output power is maximized by adjusting the OC ratio. At 27% OC, the output power reaches the maximum 42 mW at 1057 nm with 15.5% slope efficiency which is also plotted in Fig. 6. We also note that the threshold power goes up with the OC ratio from 64 mW at 17% OC to 68.5 mW at 27% OC. The output laser is found as a single mode Gaussian-like beam as indicated by the captured beam profile in the inset of Fig. 6. The output signal spectrum is also shown as another inset at the maximum signal power. The spectral width of the output signal is 2 nm with a central wavelength at 1057 nm. The signal-to-noise ratio is higher than 40 dB.

The rather low laser efficiency is attributed to a high cavity loss resulted from the free space coupling optics as schematically presented in Fig. 5. The cavity loss is estimated as 4.6 dB excluding the output coupling. All-fiberized connection would significantly reduce the coupling loss and broaden the applications of the DHAF. This is in the scope of further research. The successful demonstration of using our air core coupler in a fiber laser cavity strongly suggests feasibility of constructing an all-fiber mid-IR laser cavity using the air core coupler technology.

We explore another application of the air core fiber for ultrafast beam delivery [25]. As the DHAF supports broadband transmission, we expect full spectrum coupling of ultrafast pulses. The ultrafast laser source was a home-made mode-locked solid-state Yb:$CaYALO_4$ oscillator by using graphene as the saturable absorber [26]. The femtosecond pulses have a spectral bandwidth of 26 nm with central wavelength at 1055 nm, with a pulse repetition frequency of 113.5 MHz and a pulse duration of 47 fs. The laser delivers a single pulse energy of 2 nJ, and a pulse peak power of 43 kW. The laser pulse is coupled into the fiber under test (FUT) via a plane-convex lens with 30 mm focal length. The transmitted beam pulse from the fiber output end is then collimated by another plane-convex lens with 8 mm focal length, and subsequently directed to an auto correlator for pulse width measurement. As shown in Fig. 8(a), when the 47 fs pulse is coupled into the core 1 of a 40 cm DHAF set at a 3 dB coupling ratio, the output pulse widths from core 1 and core 2 are measured at 75 fs and 71 fs respectively, which are almost the same. Their mode profiles in Fig. 8(a) verify single mode transmission and the 3 dB coupling. We also change the coupling ratio in a range of 5 – 60% as indicated in the upper x-axis in Fig. 8(a). There is no change in the pulse width as presented by the dashed green line in Fig. 8(a), confirming robust and uncompromised operation of our coupler for ultrafast laser power splitting

Optics EXPRESS

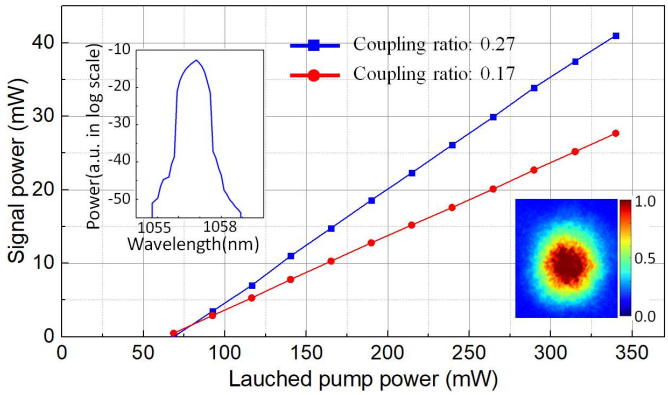

Fig. 6. Evolution of signal power as launched pump power increases with output coupling ratio, $r = 0.17$ and $r = 0.27$, respectively. Insets show the output spectrum at the maximum signal power at 27% output coupling ratio (left), and the output beam profile (right).

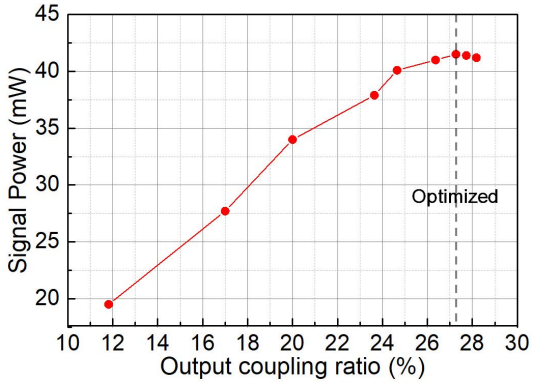

Fig. 7. Measured output signal power at various output coupling ratios under the maximum pump power.

and delivery.

The air core delivery results are compared to a commercial 62.5 μm solid core multimode fiber (MMF). A same length of the MMF piece is prepared for the transmission test. As presented in Fig. 8(b), the 47 fs input pulse experiences rapid broadening when propagating through the 40 cm MMF. The pulse broadens to 500 fs. Our theoretical values, calculated from dispersion length, L_D, and nonlinear length, L_{NL}, also indicate much broader pulse width by the MMF, as discussed more detailed in Appendix B. The calculated pulse widths are plotted in dashed curves in Fig. 8(b). We notice that actual broadening is larger than the theoretical expectation in both the DHAF and MMF. For the DHAF, the measured broadening factor is 1.60 which is a bit greater than the calculated value of 1.15. This discrepancy would be mainly caused by the overlap between propagating pulse and silica wall, which was not taken into consideration in the calculation. In fact, since the nonlinear index of silica is four orders of magnitude higher than that of air [27, 28], even 0.5% percentage light overlap with the silica can significantly enhance the nonlinear effects. For the MMF, the discrepancy is attributed to the error between actual and estimated values of simulation parameters including effective mode area, nonlinearity index, and dispersion factor (since modal dispersion was not considered in the simulation). Details of the calculation parameters are described in Appendix B.

Optics EXPRESS

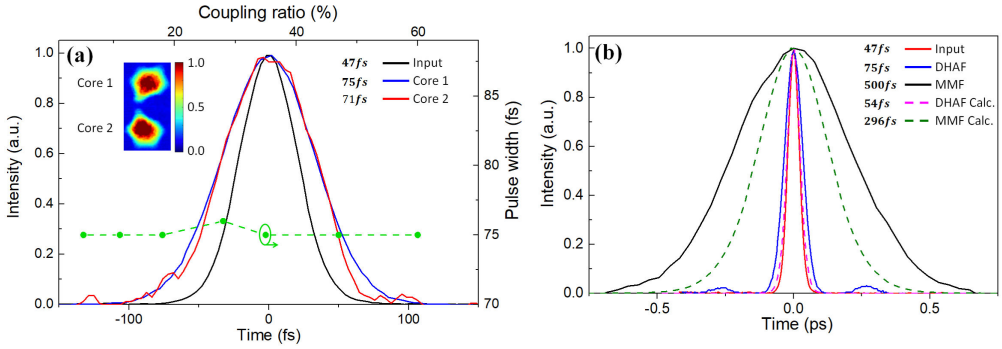

Fig. 8. (a) Input pulse vs output pulses from air core coupler; the output pulse width from the core 1 is plotted over different coupling ratio (dashed green line). The inset shows the near field mode image. (b) Output pulses from the air core coupler (blue) and a commercial MMF (black). Dashed lines present the calculated results. Input pulse is presented as the red line.

The two core structure can be utilized to build an all-fiber interferometer. Figures 9(a) and 9(b) represent the interference patterns generated by the DHAF. When the two cores carry comparable powers, an interference pattern with high contrast can be generated. On contrary, a low contrast interference pattern is generated when one core carries much larger power than the other core. Therefore, this DHAF design demonstrated a simple straightforward way to create fiber based interferometer, which might be applicable to sensors [29], quantum photonics devices [30] and optical coherence tomography [31].

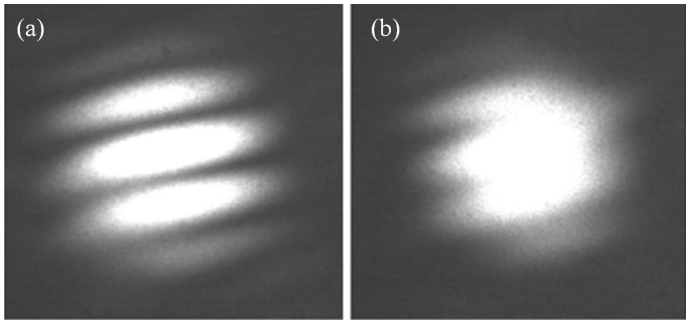

Fig. 9. Interference patterns generated by the DHAF, and captured in a far-field. (a) Strong interference when comparable power is carried at each core; (b) weak interference when carried powers at both cores are unmatched.

4. Conclusions

In conclusion, we design, fabricate and characterize a DHAF design to demonstrate air-core air-gap coupling. Each core of the DHAF performs as an anti-resonant fiber, and coupling of the anti-resonant band between two cores demonstrated. The coupler is polarization insensitive, making its adoption simpler. It also shows a unique feature of variable coupling ratio by simply applying a longitudinal strain. Its robust operation is demonstrated in a laser cavity as an output coupler and femtosecond pulse delivery and splitting. The uncompromised anti-resonant waveguide mechanism in our coupler suggests interesting applications in mid-IR and UV regions where today's fiber coupler cannot reach.

Optics EXPRESS

Appendix A: Intact transmission bands under different tensions

Figure 4 shows the variable coupling ratio of the DHAF by applying different longitudinal tension on the fiber. Figure 10 implies that the transmission bands of the DHAF can keep intact under different tensions.

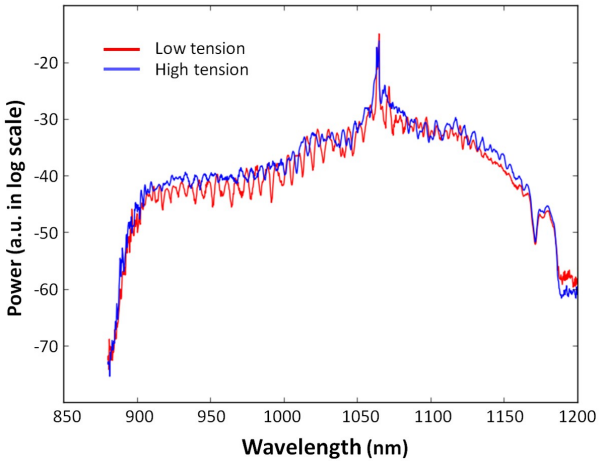

Fig. 10. Transmission spectra from core 2 of DHAF when input light is launched into core 1. The anti-resonant bands re- main intact through the various tensions.

Appendix B: Calculation of pulse broadening

We here describe our calculation of the broadened pulse as shown in Fig. 8(b). Pulse broadening is mainly induced by group velocity dispersion (GVD) and nonlinear effects [27]. The dispersion length L_D and the nonlinear length L_{NL} indicate contributions of the dispersive or nonlinear effects to pulse broadening. L_D and L_{NL} are defined as:

$$L_D = \frac{T_0^2}{|\beta_2|}, L_{NL} = \frac{1}{\gamma P_0} \tag{1}$$

where T_0 is full width at half maximum (FWHM) of an incident pulse, β_2 represents dispersion of the group velocity and is responsible for pulse broadening, P_0 is peak power of the incident pulse, and γ is the nonlinear coefficient and can be calculated by the following equation:

$$\gamma = \frac{2\pi n_2}{\lambda A_{eff}} \tag{2}$$

where n_2 is the nonlinear index of fiber core material, A_{eff} is the effective mode area, and λ is the central wavelength of the pulse. In our case, $P_0 = 43kW$, $T_0 = 47fs$, $\lambda = 1055nm$, the following table is obtained according to equation Eqs. (1) and (2). The effective mode areas in Table 2 are

Table 2. Dispersion and Nonlinear Length Calculation

Fiber Type	n_2	A_{eff}	$\lvert\beta_2\rvert$	L_{NL}	L_D
Unit	$10^{-20}cm^2/W$	μm^2	ps^2/km	m	m
MMF	2.8×10^4 [27]	655	23.3 [32]	0.087	0.095
DCAF	8.0 [28]	210	1.75	97.0	1.262

Optics EXPRESS

the simulated values by using Polymode [2] assuming that the beam is guided in the fundamental mode. The effective refractive index at 1055 *nm* of the DHAF is also calculated and fitted into the equation: $n(\lambda) = -1.768 \times 10^{-12}\lambda^3 + 5.175 \times 10^{-19}\lambda^2 - 5.599 \times 10^{-6}\lambda + 1.002$, as is plotted in Fig. 11. β_2 of DHAF is then calculated according to the formula $\beta_2 = \frac{\lambda^3}{2\pi c^2}\frac{d^2n}{d\lambda^2}$ [27].

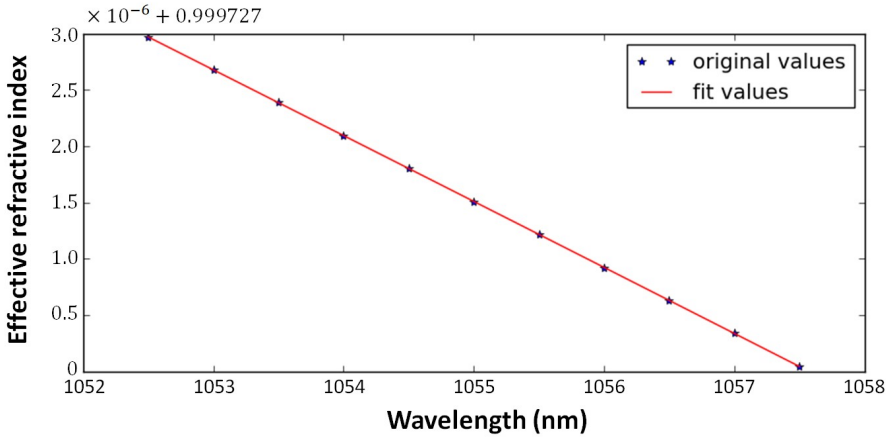

Fig. 11. Simulated and fitted value of effective index of DHAF.

In both cases, fiber length L is set at 0.4 m. The code in Appendix B in [27] based on spilt-step method is used to simulate the pulse evolution. For MMF, since $L_D < L$, $L_{NL} < L$, dispersion and nonlinearity act together as the pulse propagates along the fiber. For DHAF, since $L_D > L$, $L_{NL} >> L$, neither dispersive nor nonlinear effects play an important role in pulse propagation, and the pulse will not suffer notable degradation [27].

Funding

Korea Evaluation Institute of Industrial Technology.